The precise decoration of Pt nanoparticles with Fe oxide by atomic layer deposition for the selective hydrogenation of cinnamaldehyde

Qingmin Hu [a,b], Sen Wang [b,c], Zhe Gao [b,*], Yunqin Li [b,c], Qian Zhang [b,c], Qun Xiang [a,*], Yong Qin [b,*]

[a] NEST Lab, Department of Chemistry, Shanghai University, Shanghai 200444, PR China
[b] State Key Laboratory of Coal Conversion, Institute of Coal Chemistry, Chinese Academy of Sciences, Taiyuan 030001, PR China
[c] Graduate University of Chinese Academy of Sciences, Beijing 100039, PR China

ARTICLE INFO

ABSTRACT

The decoration of noble metal-based catalysts with metal oxides can improve their catalytic performance for the selective hydrogenation of cinnamaldehyde to cinnamyl alcohol (COL) due to the interaction between the noble metal and metal oxides. Here, we used atomic layer deposition (ALD) to decorate Pt nanoparticles precisely with Fe oxides. The selectivity to COL increased from 45% for the bare Pt catalyst to 84% for the Pt-based catalyst after 30 cycles of decoration with Fe oxide by ALD. A series of characterizations demonstrated that the precise blocking of low coordinated Pt sites with Fe oxide by ALD, generating Pt-FeO$_x$ interfacial perimeter sites, and the interaction between the Pt nanoparticles and Fe oxide led to high selectivity to COL. This precise decoration and the formation of interfacial perimeter sites by ALD provide a promising route for the design of advanced catalysts.

© 2017 Elsevier B.V. All rights reserved.

1. Introduction

The selective hydrogenation of the carbonyl bond (C═O) of α-β unsaturated aldehydes to form the corresponding unsaturated alcohols has caught the attention of researchers because these products are widely used in industry [1–3]. Cinnamaldehyde (CAL) is a typical unsaturated aldehyde [4–7]. Because of the competitive hydrogenation of the C═C and C═O bonds, the products of the hydrogenation of CAL include COL, hydrocinnamaldehyde (HCAL) and 3-phenylpropanol (HCOL) (Scheme 1). COL is widely used in fragrances, drugs and other chemicals. Pt-based catalysts are usually used in the selective hydrogenation of CAL for the preparation of COL. Significant efforts have been made to promote the selective hydrogenation of the C═O bond by Pt-based catalysts while hindering the hydrogenation of the C═C bond [3,8,9]. There are several factors that influence the catalyst selectivity to COL, such as the interfacial perimeter sites, the strong metal-support interaction (SMSI) [10,11], the geometry and size of the catalytic metal nanoparticle [11–15], and the electr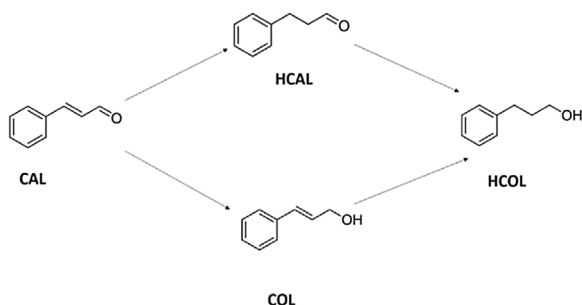onic state of the catalytic metal surface atoms [14,16,17]. The interfacial perimeter sites play a vital role in this hydrogenation reaction [18].

In recent decades, many researchers have found that different sites on the Pt nanoparticles surface influence the adsorption modes of the reactant [17,19,20]. DFT calculation demonstrated that flat surfaces, such as Pt (111), adsorb the unsaturated aldehyde in a terminal C═O mode. This mode leads the preferential terminal aldehyde to be reduced to unsaturated alcohol. Pt (100) prefers the adsorption of both C═O and C═C. Low coordinated sites (such as steps, edges, corners, and defect sites) favour π interactions with C═C, accounting for unselective product formation [21]. Smaller nanoparticles possess more low coordinated sites such as corners and edges but fewer facets than larger nanoparticles [14,22]. Decorating the low coordinated Pt sites with other species and selectively forming interfacial perimeter sites would be interesting as a way to change the selectivity to COL.

Adding another species (promoter), such as Co [17,23] or Fe [23], to Pt-based catalysts can improve their selectivity to COL. The unsaturated aldehydes adsorbed more strongly via the C═O bond in a di-σ mode at the resulting interfacial perimeter sites [24]. Furthermore, electron transfer between the added species and the Pt nanoparticles was observed [25]. The selective blockage of a metal nanoparticle surface by another species is an effective method to improve the catalytic selectivity and has been widely studied [26,27].

* Corresponding authors.
E-mail addresses: gaozhe@sxicc.ac.cn (Z. Gao), shinexq@shu.edu.cn (Q. Xiang), qinyong@sxicc.ac.cn (Y. Qin).

Scheme 1. Reaction pathways of cinnamaldehyde hydrogenation.

Atomic layer deposition (ALD) is a powerful technique for depositing nanoparticles or thin films and has outstanding advantages, including precise control of size and thickness and excellent uniformity [28–30]. ALD is also an advanced catalyst design method for improving catalytic performance [31–33]. Lu and co-workers reported that Al_2O_3 ALD was able to block low coordinated metal sites while leaving (111) facets available for the catalysis of Pd [34] (or Cu, Pt [35]) nanoparticles. In this work, different numbers of cycles of ALD Fe oxide were used to precisely decorate Pt nanoparticles. Low coordinated Pt sites were blocked. The resulting interfacial perimeter sites are more beneficial to the hydrogenation of the C=O bond than low coordinated Pt sites, increasing the selectivity to COL. After the decoration of Pt nanoparticles with ALD Fe oxide, the selectivity to COL improved from 45% to 84%.

2. Experimental Method

2.1. Catalyst synthesis

Prior to ALD, Al_2O_3 (aluminium oxide, 40–50 nm, 32–40 m²/g, NanoDur, 99.5%, Alfa Aesar Co., Ltd.) powders were dispersed in ethanol by ultrasonic agitation for ten minutes. The suspension was dropped onto quartz wafers and dried in air. Pt nanoparticles were deposited onto the Al_2O_3 supports by a hot-wall, closed-chamber ALD reactor. N_2 (99.999%) was used as carrier gas. The precursors of Pt were (methylcyclopentadienyl)trimethylplatinum (MeCpPtMe₃, Strem Chemicals, 99%) and ozone (O_3). O_3 acts as an oxidant and enables growth over a wide temperature range. The deposition temperature was 270 °C, and the MeCpPtMe₃ was kept at 60 °C. The pulse, exposure, and purge time for the MeCpPtMe₃ precursor were 0.5, 10 and 20 s, and for O_3, 1, 10 and 20 s, respectively. After the deposition of Pt nanoparticles, Fe_2O_3 ALD was subsequently deposited with ferrocene (Aladdin Chemistry Co. Ltd. 99%) and O_3 as precursors at the same temperature as for Pt ALD. The ferrocene was kept at 90 °C. The pulse, exposure, and purge time for the ferrocene precursor were 0.8, 8 and 20 s, and for O_3, 0.3, 8 and 20 s, respectively. Ultimately, the catalysts were transferred into a tube furnace and reduced at 400 °C in a H_2/Ar atmosphere for 2 h.

In this paper, the reduced Pt/Al_2O_3 catalyst produced with 30 cycles of Pt deposition is designated Pt30. The Pt-based catalysts decorated with different numbers of cycles of Fe oxide deposition by ALD are designated Pt30Fex, where x is the number of Fe oxide ALD cycles (10, 20, 30, 40 and 75, respectively). These Pt30 and Pt30Fex catalysts before reduction are designated un-Pt30 and un-Pt30Fex, respectively.

For comparison, catalysts were also prepared by traditional impregnation methods. First, Pt30 was prepared by ALD, and then the powders were impregnated with $Fe(NO)_3•9H_2O$ in solution (pH = 3) for 10 minutes with different Fe contents of 0.5%, 0.85%, and 5%. Afterwards, the solution was dried at 110 °C for 2 h and subsequently calcinated at 500 °C for 2 h in static air. The sample was also reduced at 400 °C in a H_2/Ar (5%/95%) atmosphere for 2 h. The

obtained catalysts were designated Pt30-0.5Fe-IWI, Pt30-Fe-IWI, and Pt30-5Fe-IWI, respectively.

2.2. Catalyst characterization

The contents of Pt and Fe in the catalysts were determined by an inductively coupled plasma atomic emission spectrometer (ICP-AES). Transmission electron micrographs (TEM) and high-resolution TEM (HRTEM) images were acquired with a JEOL-2100F microscope.

XRD patterns were collected on a Bruker D8 Advance X-ray diffractometer using a Cu Kα source. The N_2 sorption measurements were performed using a Micromeritics Tristar 3000 at 77 K. Prior to measurement, the samples were heated at 473 K for 1 h under vacuum to remove physisorbed water. The Brunauer−Emmett−Teller (BET) surface areas were estimated over a relative pressure (P/P_0) range of 0.04–0.32.

Temperature programmed reduction (TPR) experiments were performed with an Auto-Chem 2920 instrument, using a 50 mg sample under a 50 mL·min⁻¹ H_2 (10%)/Ar flow with a heating rate of 10 °C·min⁻¹ from room temperature to 700 °C.

Diffuse reflectance infrared Fourier transform spectroscopy (DRIFTS) data on CO adsorption were collected on a Bruker Vector 22 spectrometer with a DTGS detector. Before the experiments, the sample in the cell was dried and reduced in H_2/Ar at 400 °C for 2 h. Subsequently, the cell was cooled to room temperature (20 °C), and then the CO adsorption was carried out using CO/Ar (5%/95%) until saturated. The flow of Ar was maintained for 30 minutes to remove physically adsorbed CO, and finally, the CO chemisorption spectra were recorded with a resolution of 2 cm⁻¹ at room temperature.

X-ray photoelectron spectroscopy (XPS) data were taken on an ES-300 photoelectron spectrometer (KRATOS Analytical) using an Al Kα source (1486.6 eV).

The pulse CO chemisorption experiments on the catalysts were carried out on an Auto Chem 2920 instrument equipped with a thermal conductivity detector (TCD). Before testing, the catalyst was reduced at 400 °C for 2 h and then cooled in Ar to room temperature (298 K).

Pt L-edge absorption spectra were obtained at the BL14W1 beamline of the Shanghai Synchrotron Radiation Facility (SSRF), Shanghai Institute of Applied Physics (SINAP), China, operated at 3.5 GeV. A Si (111) double-crystal monochromator was used to reduce the harmonic component of the monochrome beam. Pt foil and PtO_2 were used as reference samples and measured in transmission mode. The Pt-based catalysts were measured in fluorescence mode.

2.3. Hydrogenation reaction

The catalytic hydrogenation of CAL (J&K Chemical, 99%) was performed in an autoclave of 100 mL with a temperature controller. In each experiment, 45 mL ethanol, 150 μL CAL and 30 mg catalyst were loaded into the reactor. The reactor was sealed and purged with purified hydrogen 3 times to remove air, and then pressurized to 2 MPa at room temperature. Subsequently, the reactor was heated to 60 °C and stirred at 700 rpm.

Disposable syringe filters were used to separate the catalyst. The liquid products collected by continuous sampling were analysed by gas chromatography-mass spectrometry (GC-MS, Agilent Technologies 7890A-5795C) with a capillary column (HP-5, 30 m × 0.25 mm × 0.25 μm).
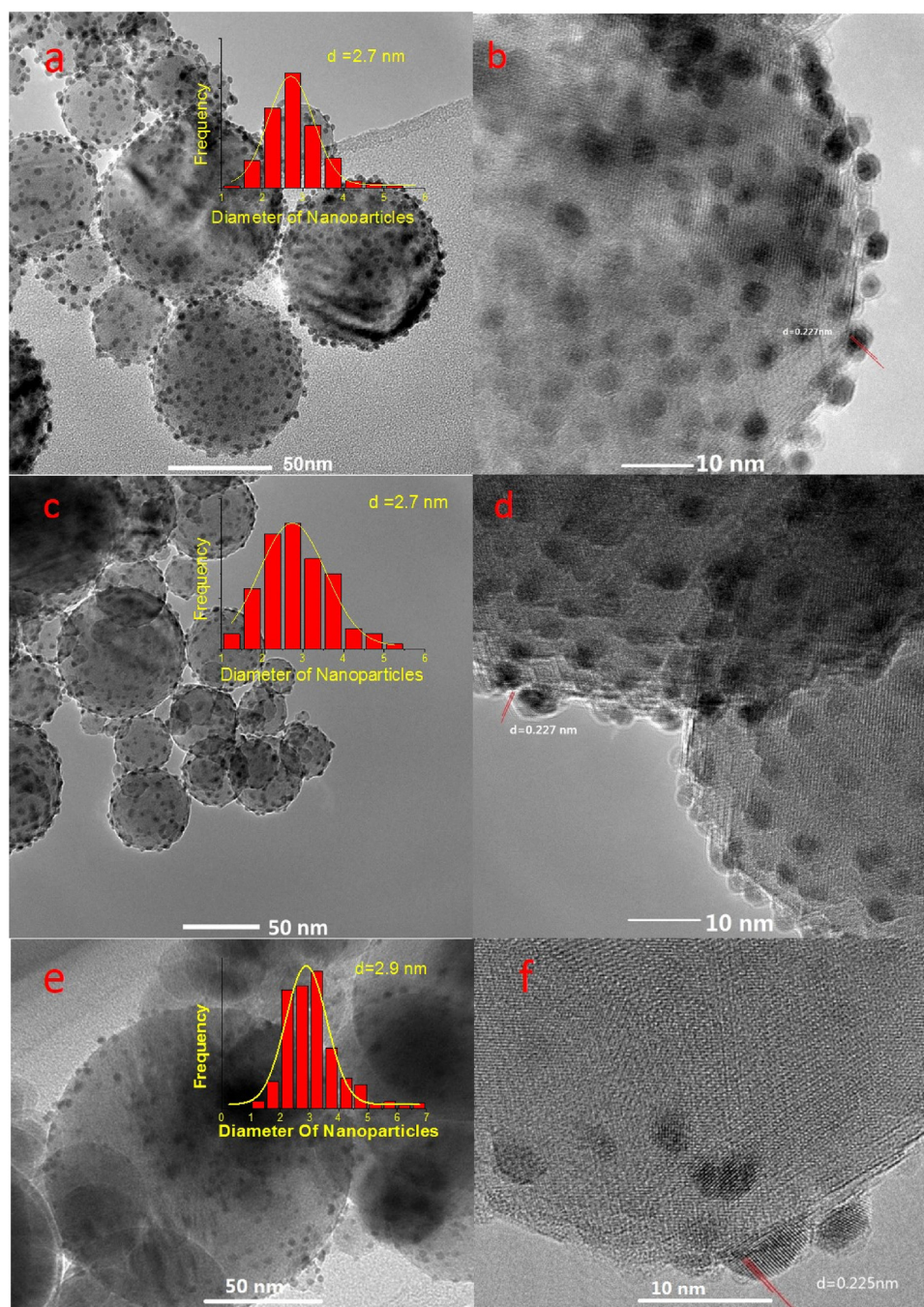
Fig. 1. TEM images of (a) Pt30, (c) Pt30Fe30, and (e) Pt30-Fe-IWI; HRTEM images of (b) Pt30, (d) Pt30Fe30, and (f) Pt30-Fe-IWI (insets in panels a, c, and e: the corresponding histograms of the particle size distribution of the catalysts).

Table 1
Pt and Fe contents of the catalysts.[a]

Sample	Pt30	Pt30Fe10	Pt30Fe20	Pt30Fe30	Pt30Fe40	Pt30Fe75
Pt/%	0.99	0.91	0.88	0.86	0.84	0.80
Fe/%	0	0.27	0.55	0.82	0.94	1.12

[a] The contents were determined with ICP-AES.

3. Results and discussion

3.1. Characterization and discussion

The contents of Pt and Fe in the catalysts were determined by ICP, as listed in Table 1. The Pt contents are 0.99% and 0.86% for Pt30 and Pt30Fe30, respectively. The Fe content for Pt30Fe30 is 0.82%. CO pulse chemisorption was further carried out to verify the numbers of surface atoms of the Pt nanoparticles. After decoration with Fe oxide, the amount of CO adsorbed by the catalyst decreased from 136.02 μmol/g (Pt30) to 14.84 μmol/g (Pt30Fe30), indicating that Fe oxide was successfully coated on the surface of the Pt nanoparticles.

It can be seen from the TEM images shown in Fig. 1a, c, and e that the Pt nanoparticles of Pt30, Pt30Fe30, and Pt30-Fe-IWI are uniformly distributed on the surface of the spherical Al_2O_3 support. The measured distances between adjacent lattice fringes are approximately 0.225 nm, which is consistent with the lattice spacing of the Pt (111) plane [22]. The Fe oxide is hardly visible in the
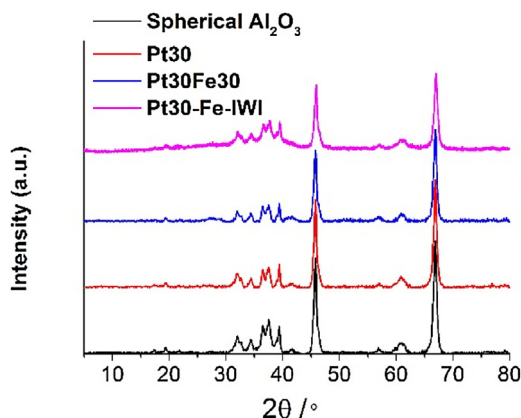
Fig. 2. XRD profiles of spherical Al_2O_3, Pt30, Pt30Fe30, and Pt30-Fe-IWI.

Fig. 3. Temperature-programmed reduction (TPR) profiles of Pt30 and Pt30Fe30 before reduction.

HRTEM images of Pt30Fe30 (Fig. 1 d) due to its low content. The mean diameters of Pt nanoparticles calculated from TEM for both Pt30 and Pt30Fe30 are 2.7 nm. These identical diameters indicate that the addition of ALD FeO_x has no influence on the diameter of the Pt nanoparticles, and thus the influence of the Pt nanoparticle size on the catalyst selectivity can be excluded. The diameter of Pt nanoparticles for Pt30-Fe-IWI is 2.9 nm. The addition of FeO_x by impregnation has little influence on the diameter of the Pt nanoparticles.

The XRD patterns of spherical Al_2O_3, Pt30, Pt30Fe30, and Pt30-Fe-IWI are presented in Fig. 2. There is no obvious difference among these XRD patterns. Only the diffraction peaks of spherical Al_2O_3 with mixed phase can be found. The diffraction peaks of Pt and Fe oxide are not observed in the XRD patterns. Their absence demonstrates that the Pt and FeO_x species are highly dispersed with small amounts.

The specific surface areas of Pt30, Pt30Fe30, and Pt30-Fe-IWI are 36.9, 38.0, and 36.8 m^2/g, respectively. In addition, the pore volumes of Pt30, Pt30Fe30, and Pt30-Fe-IWI are 0.24, 0.24 and 0.25 cm^3/g, respectively. There is little difference between the surface areas of these catalysts, and their pore volumes are almost identical.

The reducibility of unreduced Pt30 and unreduced Pt30Fe30 were determined by temperature programmed reduction (TPR), as shown in Fig. 3. There are two peaks in the TPR profile of un-Pt30. A small peak appears at 91 °C, and a large principal peak is located at 410 °C. The TPR profile of un-Pt30Fe30 displays peaks at 56 °C, 360 °C and 410 °C. The peaks below 100 °C in the two patterns are attributed to reduction of the Pt oxidized species. The strong peak at 410 °C in the two TPR profiles may result from the strong interaction between the Pt nanoparticles and the support [36]. The peak at 360 °C in the pattern of un-Pt30Fe30 can be attributed to the reduc-
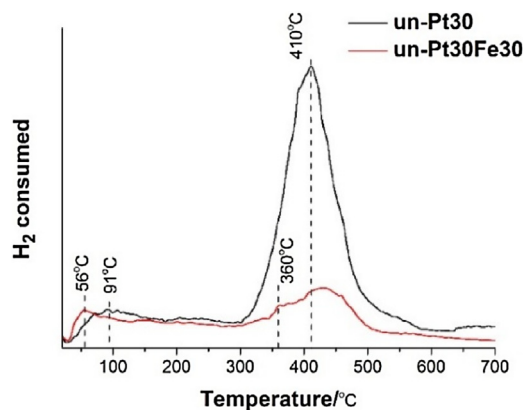
tion of Fe_2O_3 to Fe_3O_4 [37]. Decoration with Fe oxide decreases the intensity of the peak at 410 °C. This result reveals the strong interaction between the Pt nanoparticles and the deposited Fe oxide.

XPS was used to study the surface electronic properties of the catalysts. An overlapping phenomenon was observed between Al 2p and Pt 4f; thus, Pt 4d was taken into account. The Pt 4d XPS spectra of Pt30, Pt30Fe30 and Pt30-Fe-IWI are displayed in Fig. 4a. It can be seen that the Pt 4d shifts to lower binding energies of 0.35 eV and 0.05 eV for Pt30Fe30 and Pt30-Fe-IWI, respectively. The peak shifts demonstrate changes in the electronic environment, indicating the interaction of Pt and FeO_x. To further reveal the Pt state, the Pt 4d spectra were fitted, as shown in Fig. 4b and c. The Pt $4d_{5/2}$ peaks at 314.3, 317.3 and 318.1 eV can be attributed to Pt^0, Pt^{2+} and Pt^{4+} species, respectively [38,39]. The percentage of Pt^0 species for Pt30Fe30 and Pt30-Fe-IWI is much higher than for Pt30. Here, FeO_x may act as a protective layer against Pt oxidation. The XPS results further confirm the stronger interaction between Pt and Fe oxide in Pt30Fe30.

X-ray absorption fine structure (XAFS) measurements were also employed to characterize the samples. From the X-ray absorption near-edge structure (XANES) spectra of Pt30 and Pt30Fe30 (Fig. 5a), it can be seen that the intensity of the white line peak for Pt30 is higher than that of the one for Pt30Fe30 [40]. This difference in intensity demonstrates that Pt30Fe30 possesses more metallic Pt species than Pt30. This difference may be due to the decoration of Fe oxide on the Pt nanoparticles, protecting the Pt nanoparticles from oxidization upon transfer of the samples to the XAFS beamline. The extended X-ray absorption fine structure spectra (EXAFS) of the catalysts are displayed in Fig. 5b. The radial distance of the Pt-Pt shell of Pt30Fe30 is shorter than that of Pt30 (consistent with the fitting results displayed in Table 2), which can be ascribed to the

Table 2
FT-EXAFS parameters of Pt foil, PtO_2, Pt30, and Pt30Fe30 samples.

sample	shell	R (Å)[a]	CN[b]	$\Delta\sigma^2 \times 10^3$ (Å²)[c]	ΔE_0 (eV)[d]
Pt30	Pt-Pt (Pt)	2.75	8.7	11.8	7.0
	Pt-Pt (Pt)	3.90	4.4	11.8	7.0
	Pt-O (PtO_2)	2.00	2.4	7.5	8.3
Pt30Fe30	Pt-Pt (Pt)	2.71	11.7	10.5	5.0
	Pt-Pt (Pt)	3.86	5.8	10.5	5.0
	Pt-O (PtO_2)	1.96	0.1	14.3	7.5
PtO_2	Pt-O	2.02	6		
Pt foil	Pt-Pt	2.77	12		
	Pt-Pt	3.91	6		

[a] R, bonding distance.
[b] CN, coordination number.
[c] $\Delta\sigma^2$, Debey-Waller factor.
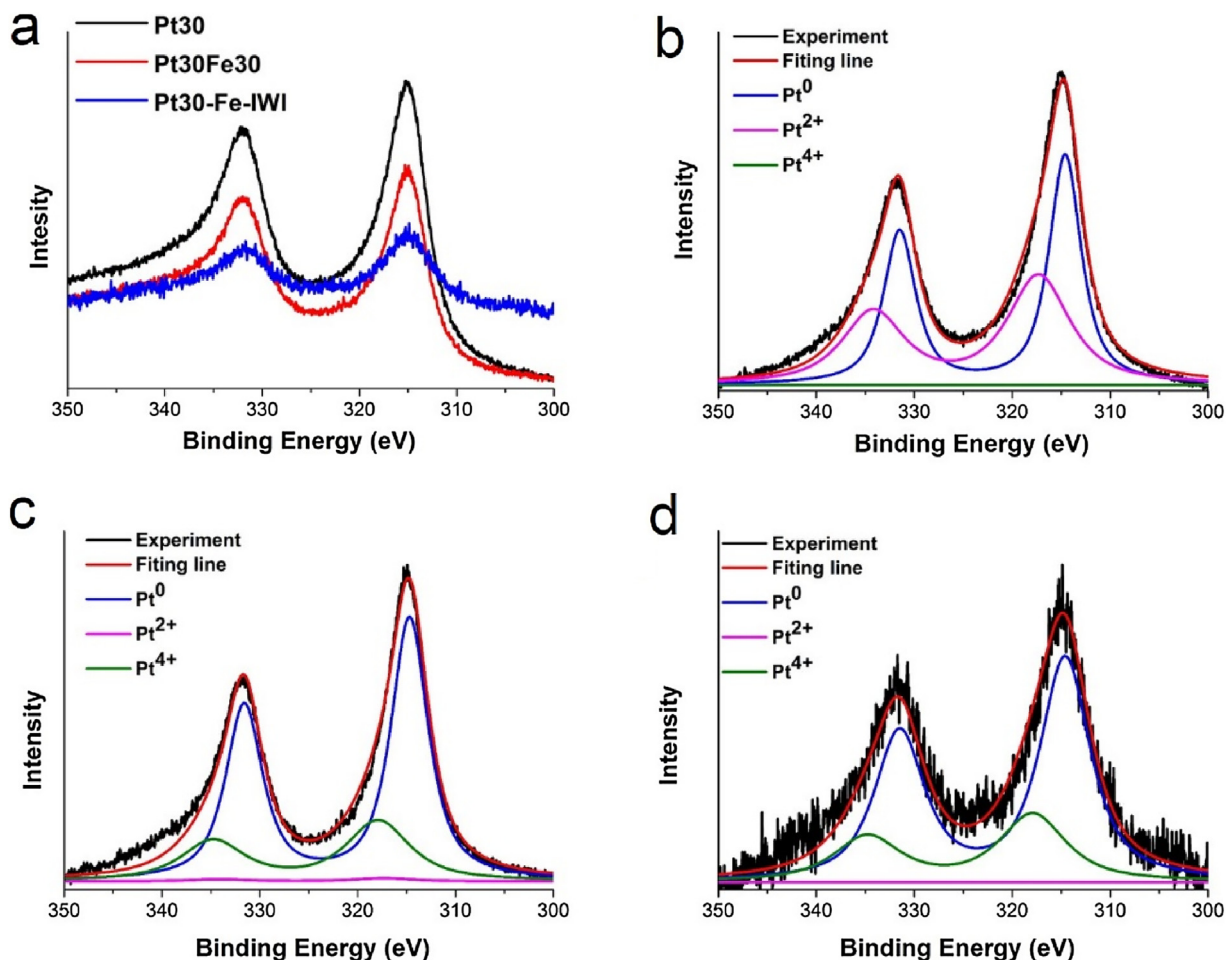[d] ΔE_0, inner potential shift.

Fig. 4. (a) Pt 4d XPS spectra of Pt30, Pt30Fe30 and Pt30-Fe-IWI; curve fits of the XPS spectra of (b) Pt30, (c) Pt30Fe30, and (d) Pt30-Fe-IWI.
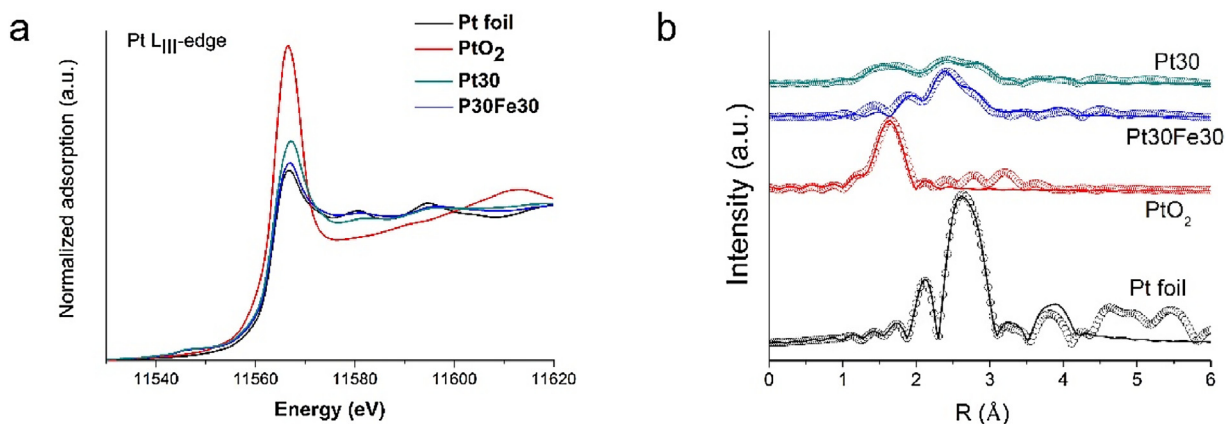

Fig. 5. (a) Pt L_{III}-edge XANES and (b) Pt L_{III}-edge k^3-weighted FT-EXAFS spectra of Pt foil, PtO_2, Pt30 and Pt30Fe30 (open circles indicate experimental data, and lines indicate fitted results).

strong interaction between the Pt and Fe oxide in Pt30Fe30. Our result is consistent with this inner shell variation induced by the surface modification reported by S. Tsang et al. [27]. These results reveal more clearly the interaction between the Pt and the added Fe oxide.

DRIFTS was carried out to investigate the surface properties of the catalysts [41]. The CO chemisorption spectra of Pt30, Pt30Fe30, and Pt30-Fe-IWI are displayed in Fig. 6a. It can be seen that the spectrum of Pt30 has two peaks centred at 2054 cm^{-1} and 1810 cm^{-1},

which can be attributed to CO species linearly absorbed and bridge-absorbed on the Pt atoms [10,42], respectively. For Pt30Fe30 and Pt30-Fe-IWI, the CO linear adsorption peak can also be seen at 2048 cm^{-1} and 2052 cm^{-1}, respectively. Compared with the Pt30 spectrum, a wavenumber decrease (redshift) of 6 cm^{-1} for the linear CO adsorption can be seen in the Pt30Fe30 spectra. The vanishing of the bridged CO adsorption peak may be caused by the addition of the Fe oxide [43].
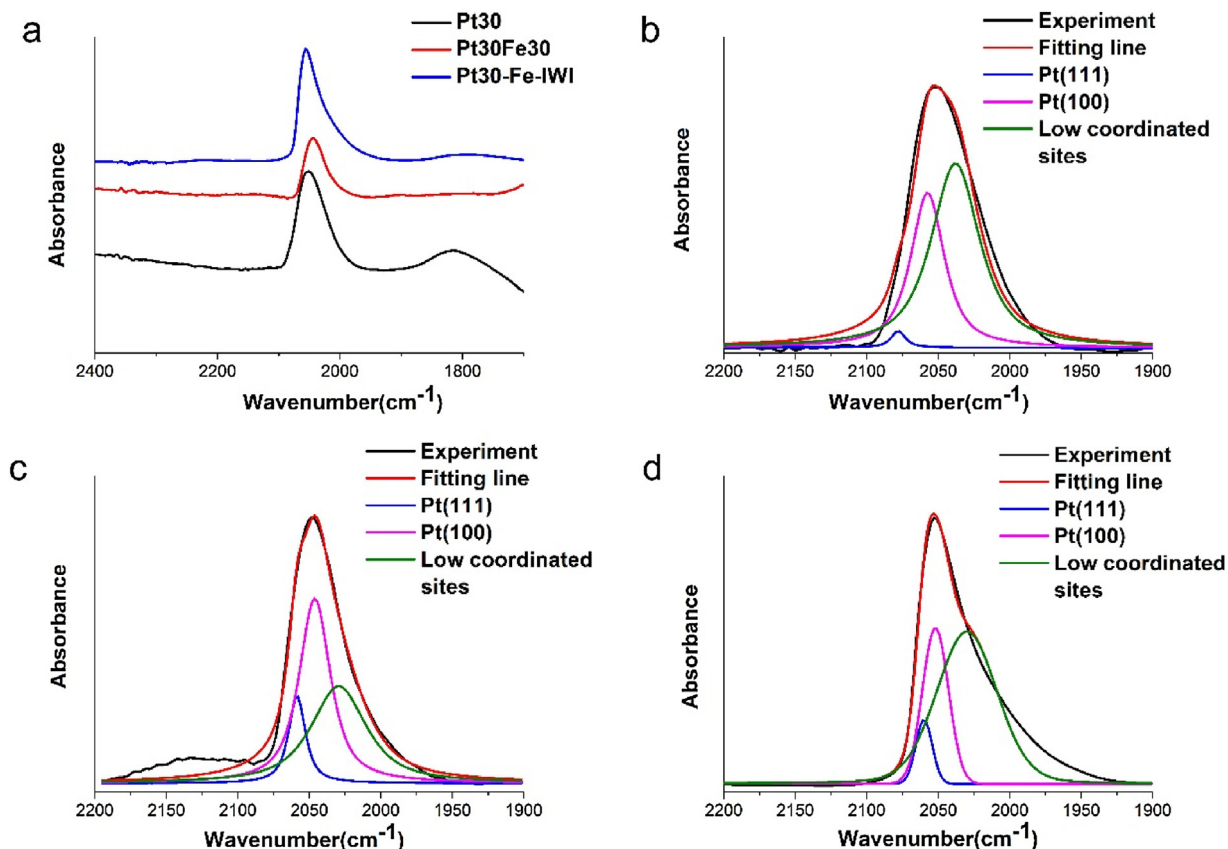
Fig. 6. (a) DRIFTS spectra of CO chemisorption of Pt30 and Pt30Fe30, and fitting curves of linear CO adsorption for (b) Pt30, (c) Pt30Fe30, and (d) Pt30-Fe-IWI.
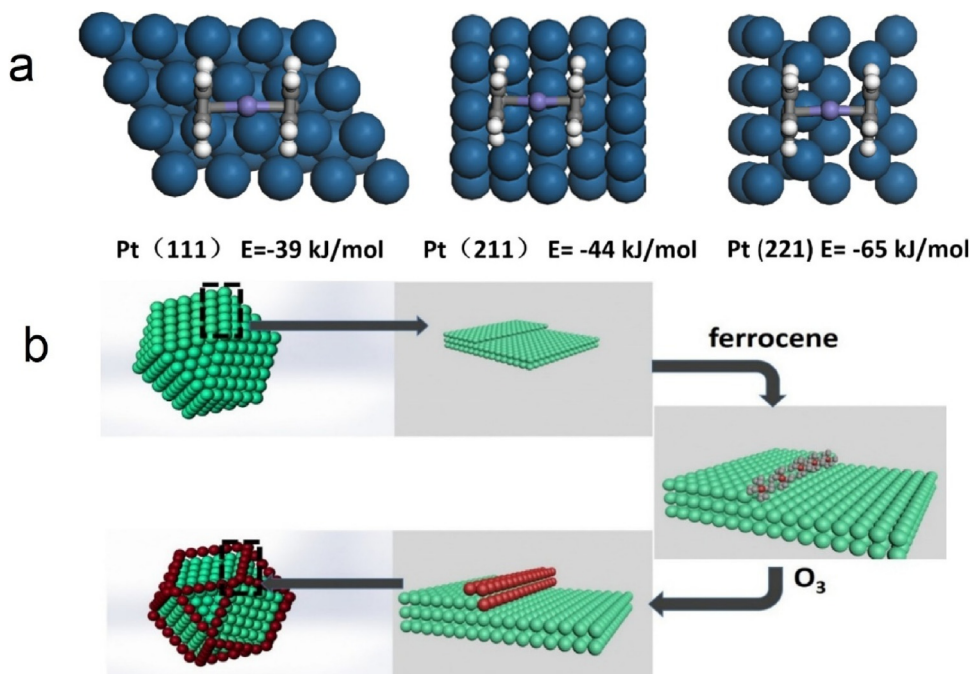

Fig. 7. (a) The adsorption energy of ferrocene located at the facet (111), step (211), and corner (221) of the Pt surface is calculated by periodic-DFT. (b) The schematic for the decoration of Pt nanoparticles with Fe oxide by ALD.

Fitting curves of linear adsorption DRIFTS of Pt30, Pt30Fe30, and Pt30-Fe-IWI are displayed in Fig. 6b, c, and d. The curves are separated into three peaks: CO adsorption on the Pt (111) facet, on the Pt (100) facet, and at low coordinated Pt sites, such as steps, edges, corners, and defect sites [42,44,45]. In the DRIFTS spectrum of Pt30,

the signals at 2079, 2057, and 2038 cm^{-1} can be attributed to linear CO adsorption on the Pt (111), Pt (110), and low coordinated Pt sites, respectively. As to the spectrum of Pt30Fe30 and Pt30-Fe-IWI, the peaks at 2058, 2046, and 2031 cm^{-1} could be ascribed to the CO linear adsorption on Pt (111), Pt (110), and low coordinated
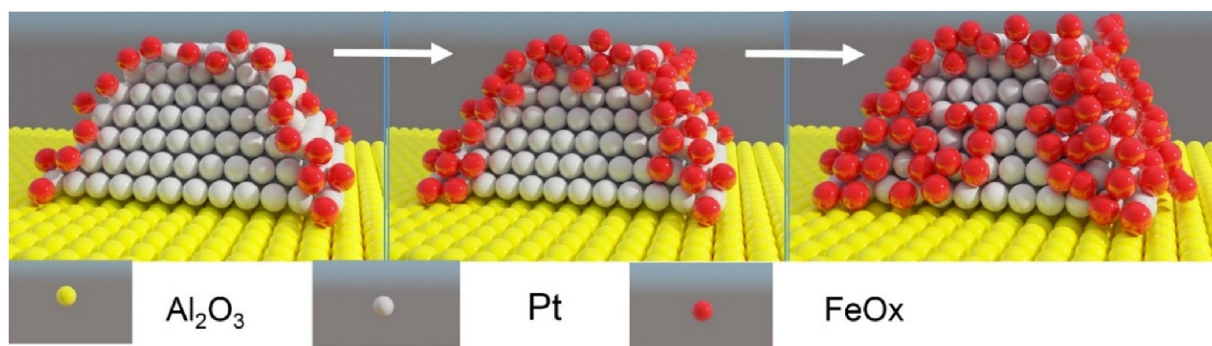
Fig. 8. Scheme of the evolution process of Pt-FeO$_x$ interfacial sites with increasing ALD cycle numbers.

Pt sites [45–48], respectively. Compared with the spectrum of Pt30, the decrease (redshift) in wavenumber for Pt30Fe30 and Pt30-Fe-IWI is mainly caused by the addition of Fe oxide to the surface of the Pt nanoparticles, which changes the electron density of the surface Pt atoms [46]. From Fig. 6b-d, it can be concluded that the percentage of low coordinated Pt sites of Pt30Fe30 is obviously lower than that of Pt30 and Pt30-Fe-IWI. This result demonstrates that the low coordinated Pt sites have been blocked selectively by FeO$_x$ ALD.

To further reveal the selective decoration of Fe oxide on the Pt surface sites, density functional theory (DFT) calculation was performed. The interaction of ferrocene located at different Pt sites was simulated through calculation of the relative energies of ferrocene located at the (111), (211) and (221) surfaces. The relative energies of the facet, step and corner sites of the Pt surfaces were compared by selecting the (111), (211) and (221) facets to represent surface configuration features. A slab of 3-layer, p(3 × 3) unit cells was used for different surfaces of Pt, and all the layers were allowed to relax.

The calculation was performed by periodic-DFT within the generalized gradient approximation (GGA) using the Vienna Ab Initio Simulation Package (VASP). The Perdew, Burke, and Ernzrhof (PBE) exchange-correlation functional was applied, and the projected augmented wave (PAW) method was employed to represent the electron−ion interactions. The kinetic energy cutoff for a plane wave basis set was 400 eV. We applied Monkhorst Pack mesh k-points of (3 × 3 × 1) for the different surfaces of Pt, allowing convergence of the total electronic energy to 0.1 meV and of the remaining total force below 0.05 eV/Å. The D2 correction of Grimme was applied to account for dispersion interactions not included in density functional theory. The relative energy of ferrocene located on the different surfaces is defined as:

$$\Delta E_{ads} = E_{adsorbate+surface} - (E_{adsorbate} + E_{surface}),$$

where $E_{adsorbate+surface}$ is the total energy of the composite system, $E_{surface}$ is the energy of the clean surface of Pt, and $E_{adsorbate}$ is the energy of isolated ferrocene. The result of the DFT calculation is shown in Fig. 7a. It can be concluded that the preferred order for ferrocene adsorption is as follows: Pt (221) > Pt (211) > Pt (111). That is, ferrocene preferentially adsorbs at the low coordinated Pt sites, which possess lower energy. The ferrocene was located on the surface of Pt nanoparticles by chemisorption and reacted in situ when O$_3$ was pulsed in, which led to the precise control advantages of ALD, as displayed in Fig. 6b.

3.2. Catalytic performance

The catalytic performances of the Pt30 and Pt30Fex catalysts prepared by ALD were evaluated. Apart from COL, CAL, and HCAL, no other products were found. Fig. 9a and b show the CAL conversion and selectivity to COL of different catalysts in the CAL hydrogenation reaction. The conversion of Pt30 after reaction for 8 h was 85%.

Table 3
The catalytic performances of impregnated catalysts.[a]

	Pt30	Pt30-0.5Fe-IWI	Pt30-Fe-IWI[b]	Pt30-5Fe-IWI
Conversion/%	85	65	58	39
Selectivity/%	47	59	62	64

[a] Reaction conditions: 30 mg catalyst, 700 rpm, 150 μL CAL, 60 °C, 2 MPa, 8 h.
[b] Pt30-Fe-IWI has the same Fe content as Pt30Fe30.

The cinnamaldehyde/Pt ratio of Pt30 was higher than that of the catalysts reported in the literature [10,49], which can be attributed to its higher Pt dispersion. The conversion decreases with increasing Fe$_2$O$_3$ ALD cycles. After reaction for 8 h, the conversions of Pt30Fe10, Pt30Fe20, Pt30Fe30, Pt30Fe40, Pt30Fe75 were 80%, 78%, 75%, 59%, and 49%, respectively. However, the selectivity to COL did not show a linear relationship with Fe oxide cycles. As shown in Fig. 9b, it displays an increasing trend within 30 ALD cycles and a decreasing trend after 30 ALD cycles. The selectivity of the Pt30Fe30 catalyst reached up to 84%, nearly twice as high as the selectivity of the Pt30 catalyst.

For comparison, catalysts were also prepared by the traditional impregnation method. Their catalytic performances are displayed in Table 3. It can be observed that the conversion of the catalysts decreased with increasing Fe content, while the selectivity to COL increased slightly. The catalytic performance of the impregnated catalyst Pt30-Fe-IWI with the same Fe amount as Pt30Fe30 prepared by ALD is also displayed in Fig. 9. The conversion and selectivity of Pt30-Fe-IWI were lower than those of Pt30Fe30. For straightforward comparison with the catalysts prepared by impregnation, Pt30 samples decorated with 30 cycles of ALD FeO$_x$ were first calcinated in air at 500 °C for 2 h, and then reduced at 400 °C in H$_2$/Ar for 2 h. The conversion (78%) and selectivity (89%) to COL are slightly higher than those of Pt30Fe30 (75% and 84%) after reaction for 8 h. This improvement may be caused by the possible sintering effect of Pt nanoparticles at 500 °C.

The product distribution of Pt30Fe30 with reaction time is shown in Fig. 9c. COL was the main product, HCOL emerged after 300 minutes, and the amount of HCAL was less than 10% during the reaction period. In addition, the stability of Pt30Fe30 was tested, as shown in Fig. 9d. The conversion of CAL was 72% for the first run and 71.92% for the fifth run. The selectivity to COL was 85.8% for the first run and 85% for the fifth run. ICP characterization was performed to analyse the Pt and Fe contents of the reused catalysts. The Pt and Fe contents of Pt30Fe30 showed little change after five runs. These results show that the catalysts exhibit excellent stability.

In this work, with increasing Fe$_2$O$_3$ ALD cycles, the CAL conversion decreases. The selectivity to COL displays an increasing trend within 30 ALD cycles and a decreasing trend after 30 ALD cycles. The evolution process of Pt-FeO$_x$ interfacial sites with increasing ALD cycle numbers is shown in Fig. 8. For the first few cycles, FeO$_x$ decorates the low coordinated sites and forms interfacial perimeter
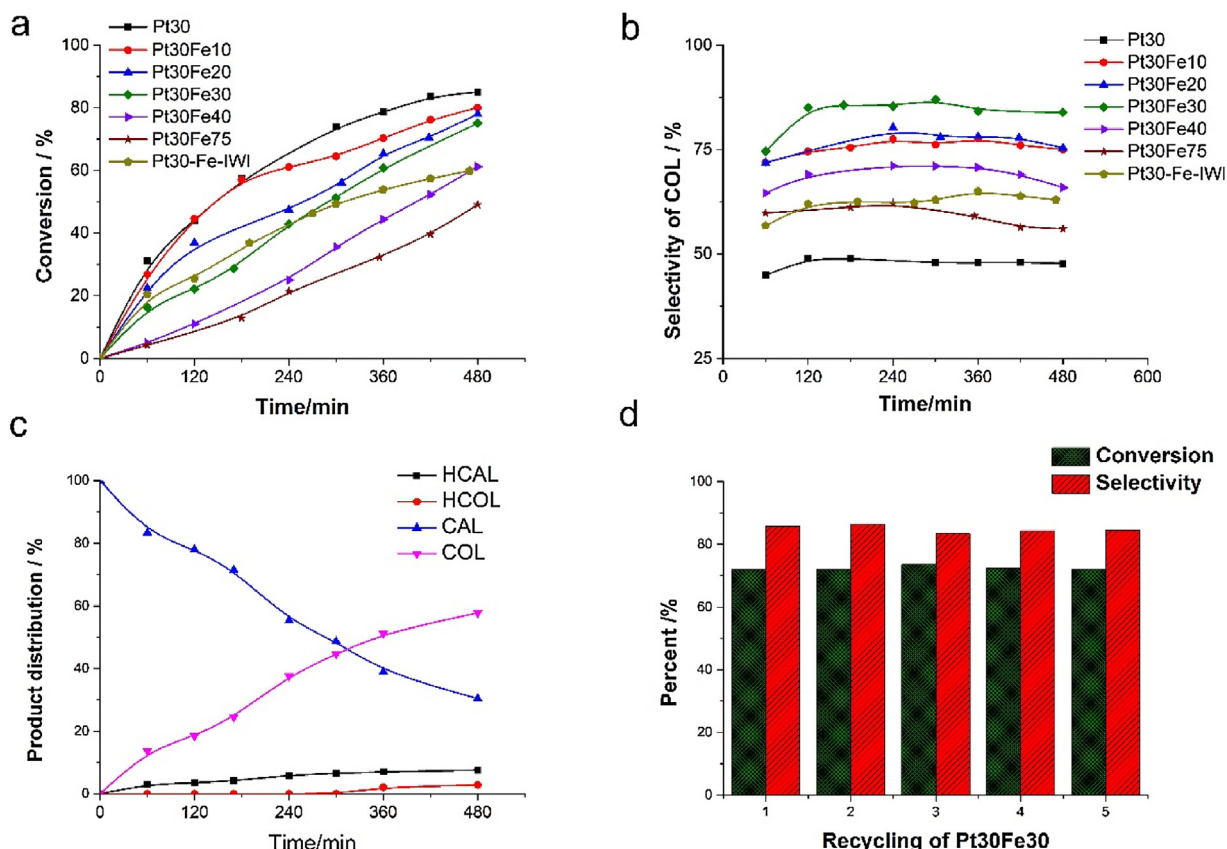
Fig. 9. (a) Conversion of CAL and (b) selectivity to COL over catalysts with reaction time, (c) the product distribution of Pt30Fe30, and (d) the recycling results of Pt30Fe30.

sites. The highly active low coordinated sites are blocked by FeO$_x$, and the formed interfacial perimeter sites are lower in number than the blocked Pt sites, decreasing the catalytic activity. Meanwhile, the decrease in low coordinated sites (which favour the C=C bond) and the formation of the interfacial perimeter sites (which favour the C=O bond) lead to increased selectivity. With increasing cycle numbers, FeO$_x$ will be deposited on flat surface sites, further increasing the interfacial perimeter sites. The concentration of interfacial perimeter sites will reach a maximum at 30 cycles, corresponding to the vertex of the volcanic selectivity curves. After further increases in cycle number over 30, the formation of a continuous Fe$_2$O$_3$ film will decrease the concentration of the interfacial perimeter sites, leading to decreased selectivity. For the catalyst prepared by the traditional impregnation method, the interaction between Pt nanoparticles and Fe oxide still occurs. However, the selectivity of the catalyst prepared by the traditional impregnation method (Pt30-Fe-IWI, 62%) is much lower than that of the catalyst prepared by ALD (Pt30Fe30, 84%). In the traditional impregnation method, all of the Pt active sites are simultaneously blocked. The precise decoration process is difficult to achieve by the traditional impregnation method.

4. Conclusion

In this study, we prepared Pt-based catalysts decorated with Fe oxide by different numbers of cycles of ALD. Among all the prepared Pt-based catalysts, the Pt30Fe30 catalyst possesses the highest selectivity to COL, two times as high as that of Pt30. HRTEM, TPR, XPS, ICP, DRIFTS, XANES and EXAFS were employed to characterize Pt30 and Pt30Fe30. The TPR, XPS, and XAFS results confirm the interactions between Pt nanoparticles and Fe oxide. The DFT calculation and DRIFTS results demonstrate that low coordinated

Pt sites were selectively blocked by ALD Fe oxide. The precise decoration of Pt sites by ALD Fe oxide and the formation of interfacial perimeter sites between Pt nanoparticles and Fe oxide led to the higher selectivity of Pt30Fe30 to COL. The precise decoration of metal nanoparticle sites by ALD offers a method to design advanced metal catalysts.

Conflict of interest

The authors declare that there are no competing financial interests.

References

[1] P. Mäki-Arvela, J. Hájek, T. Salmi, D.Y. Murzin, Appl. Catal. A: Gen. 292 (2005) 1–49.
[2] J. Shi, M. Zhang, W. Du, W. Ning, Z. Hou, Catal. Sci. Technol. 5 (2015) 3108–3112.
[3] J. Shi, R. Nie, P. Chen, Z. Hou, Catal. Commun. 41 (2013) 101–105.
[4] Z. Wang, K.-D. Kim, C. Zhou, M. Chen, N. Maeda, Z. Liu, J. Shi, A. Baiker, M. Hunger, J. Huang, Catal. Sci. Technol. 5 (2015) 2788–2797.
[5] W. Yu, Y.-P. Hsu, C.-S. Tan, Appl. Catal. B: Environ. 196 (2016) 185–192.
[6] C. Piqueras, V. Puccia, D. Vega, M. Volpe, Appl. Catal. B: Environ. 185 (2016) 265–271.
[7] R. Nie, M. Miao, W. Du, J. Shi, Y. Liu, Z. Hou, Appl. Catal. B: Environ. 180 (2016) 607–613.

[8] K.R. Kahsar, D.K. Schwartz, J.W. Medlin, J. Mol. Catal. A: Chem. 396 (2015) 188–195.
[9] B.F. Machado, S. Morales-Torres, A.F. Pérez-Cadenas, F.J. Maldonado-Hódar, F. Carrasco-Marín, A.M.T. Silva, J.L. Figueiredo, J.L. Faria, Appl. Catal. A: Gen. 425–426 (2012) 161–169.
[10] S. Handjani, E. Marceau, J. Blanchard, J.-M. Krafft, M. Che, P. Mäki-Arvela, N. Kumar, J. Wärnå, D.Y. Murzin, J. Catal. 282 (2011) 228–236.
[11] X. Ji, X. Niu, B. Li, Q. Han, F. Yuan, F. Zaera, Y. Zhu, H. Fu, ChemCatChem 6 (2014) 3246–3253.
[12] E. Bus, R. Prins, J.A. van Bokhoven, Catal. Commun. 8 (2007) 1397–1402.
[13] H. Mistry, F. Behafarid, S.R. Bare, B. Roldan Cuenya, ChemCatChem 6 (2014) 348–352.
[14] W.O. Oduro, N. Cailuo, K.M. Yu, H. Yang, S.C. Tsang, Phys. Chem. Chem. Phys. 13 (2011) 2590–2602.
[15] I. Lee, F. Delbecq, R. Morales, M.A. Albiter, F. Zaera, Nat. Mater. 8 (2009) 132–138.
[16] A. Da Silva, E. Jordao, M. Mendes, P. Fouilloux, Appl. Catal. A: Gen. 148 (1997) 253–264.
[17] R. Zheng, M.D. Porosoff, J.L. Weiner, S. Lu, Y. Zhu, J.G. Chen, Appl. Catal. A: Gen. 419 (2012) 126–132.
[18] Z. Guo, C. Zhou, D. Shi, Y. Wang, X. Jia, J. Chang, A. Borgna, C. Wang, Y. Yang, Appl. Catal. A: Gen. 435–436 (2012) 131–140.
[19] A.J. Urquhart, F.J. Williams, O.P. Vaughan, R.L. Cropley, R.M. Lambert, Chem. Commun. (2005) 1977–1979.
[20] M.S. Ide, B. Hao, M. Neurock, R.J. Davis, ACS Catal. 2 (2012) 671–683.
[21] F. Delbecq, P. Sautet, J. Catal. 152 (1995) 217–236.
[22] D. Wang, Y. Zhu, C. Tian, L. Wang, W. Zhou, Y. Dong, Q. Han, Y. Liu, F. Yuan, H. Fu, Catal. Sci. Technol. 6 (2016) 2403–2412.
[23] Z. Guo, Y. Chen, L. Li, X. Wang, G.L. Haller, Y. Yang, J. Catal. 276 (2010) 314–326.
[24] A. Dandekar, M.A. Vannice, J. Catal. 183 (1999) 344–354.
[25] J. Hidalgo-Carrillo, M.A. Aramendía, A. Marinas, J.M. Marinas, F.J. Urbano, Appl. Catal. A: Gen. 385 (2010) 190–200.
[26] J. Zhang, M. Ibrahim, V. Collière, H. Asakura, T. Tanaka, K. Teramura, K. Philippot, N. Yan, J. Mol. Catal. A: Chem. 422 (2016) 188–197.
[27] S. Jones, S. Fairclough, M. Gordon-Brown, W. Zheng, A. Kolpin, B. Pang, W. Kuo, J. Smith, S. Tsang, Chem. Commun. 51 (2015) 46–49.
[28] R. Paul, R.G. Reifenberger, T.S. Fisher, D.Y. Zemlyanov, Chem. Mater. 27 (2015) 5915–5924.
[29] L. Baker, A.S. Cavanagh, D. Seghete, S.M. George, A.J.M. Mackus, W.M.M. Kessels, Z.Y. Liu, F.T. Wagner, J. Appl. Phys. 109 (2011) 084333.
[30] Z. Gao, M. Dong, G. Wang, P. Sheng, Z. Wu, H. Yang, B. Zhang, G. Wang, J. Wang, Y. Qin, Angew. Chem. Int. Ed. 54 (2015) 9006–9010.
[31] E. Sairanen, R. Karinen, M. Borghei, E.I. Kauppinen, J. Lehtonen, ChemCatChem 4 (2012) 2055–2061.
[32] H. Ge, B. Zhang, X. Gu, H. Liang, H. Yang, Z. Gao, J. Wang, Y. Qin, Angew. Chem. Int. Ed. 55 (2016) 7081–7085.
[33] J. Li, B. Zhang, Y. Chen, J. Zhang, H. Yang, J. Zhang, X. Lu, G. Li, Y. Qin, Catal. Sci. Technol. 5 (2015) 4218–4223.
[34] J. Lu, B. Fu, M.C. Kung, G. Xiao, J.W. Elam, H.H. Kung, P.C. Stair, Science 335 (2012) 1205–1208.
[35] J. Lu, B. Liu, N.P. Guisinger, P.C. Stair, J.P. Greeley, J.W. Elam, Chem. Mater. 26 (2014) 6752–6761.
[36] J.E. Park, B.B. Kim, E.D. Park, Korean J. Chem. Eng. 32 (2015) 2212–2219.
[37] P.-F. Qu, J.-G. Chen, Y.-H. Song, Z.-T. Liu, Z.-W. Liu, Y. Li, J. Lu, J. Jiang, Catal. Commun. 68 (2015) 105–109.
[38] A.V.-H. Soares, G. Perez, F.B. Passos, Appl. Catal. B: Environ. 185 (2016) 77–87.
[39] A. Fernández, G. Arzac, U. Vogt, F. Hosoglu, A. Borgschulte, M.J. de Haro, O. Montes, A. Züttel, Appl. Catal. B: Environ. 180 (2016) 336–343.
[40] O. Neufeld, M.C. Toroker, J. Phys, Chem. C 119 (2015) 5836–5847.
[41] E.A. Redina, O.A. Kirichenko, A.A. Greish, A.V. Kucherov, O.P. Tkachenko, G.I. Kapustin, I.V. Mishin, L.M. Kustov, Catal. Today 246 (2015) 216–231.
[42] A. Moscu, L. Veyre, C. Thieuleux, F. Meunier, Y. Schuurman, Catal. Today 258 (2015) 241–246.
[43] A. Satsuma, T. Tojo, K. Okuda, Y. Yamamoto, S. Arai, J. Oyama, Catal. Today 242 (2015) 308–314.
[44] Y. Li, M. Shen, J. Wang, T. Wan, J. Wang, Catal. Sci. Technol. 5 (2015) 1731–1740.
[45] F. Hoxha, B. Schimmoeller, Z. Cakl, A. Urakawa, T. Mallat, S.E. Pratsinis, A. Baiker, J. Catal. 271 (2010) 115–124.
[46] S. Kobayashi, M.-a. Kaneko, H. Ohshima, H. Kurokawa, Appl. Catal. A: Gen. 417–418 (2012) 306–312.
[47] E. Schmidt, W. Kleist, F. Krumeich, T. Mallat, A. Baiker, Chemistry 16 (2010) 2181–2192.
[48] A.S. Barnard, Comput. Phys. Commun. 182 (2011) 11–13.
[49] A.B. Merlo, B.F. Machado, V. Vetere, J.L. Faria, M.L. Casella, Appl. Catal. A: Gen. 383 (2010) 43–49.